PERGAMON

International Journal of Heat and Mass Transfer 45 (2002) 3781–3793

International Journal of HEAT and MASS TRANSFER

www.elsevier.com/locate/ijhmt

Non-Darcy natural convection in high porosity metal foams

M.S. Phanikumar [a,*], R.L. Mahajan [b]

[a] *Departments of Civil and Environmental Engineering and Geological Sciences, Michigan State University, East Lansing, MI 48824, USA*

[b] *CAMPMode (Center for Advanced Manufacturing and Packaging of Microwave, Optical and Digital Electronics), Department of Mechanical Engineering, University of Colorado, Boulder, CO 80309, USA*

Received 23 March 2001; received in revised form 16 February 2002

Abstract

We present numerical and experimental results for buoyancy-induced flows in high porosity metal foams heated from below. A Brinkman–Forchheimer-extended Darcy flow model and a semi-heuristic two-equation energy model obtained by relaxing the local thermal equilibrium (LTE) assumption are adopted. Experiments conducted under natural convection conditions for the same configuration are used to test the numerical model and the validity of the thermal equilibrium assumption for metal foams. Aluminum foam samples of different pore sizes (5–40 PPI) and porosities ($0.89 \leqslant \varepsilon \leqslant 0.97$) are used to illustrate the effects of metal foam geometry on heat transfer. In addition, several metal foam–fluid combinations (aluminum–air, carbon–air, aluminum–water, and nickel–water) are used to study the heat transfer enhancement relative to the base case in which there is no metal foam but only a heated plate. Thermal dispersion effects and the effects of Darcy number on heat transfer are reported. Our results indicate that the thermal non-equilibrium model provides a superior description of heat transfer in metal foams, especially in the presence of fluid–porous interfaces.

Keywords: Porous media; Metal foams; Natural convection; Enhancement; Local thermal non-equilibrium

1. Introduction

Flow and transport at the interface between a porous medium and a clear fluid are of interest in a variety of engineering applications as well as in the environment. Solidification processes, thermal insulation, heat pipes, the interaction of groundwater with surface water and solute exchange in the hyporheic zone are some such examples. This paper deals with fluid flow and heat transfer in metal foams in the presence of fluid–porous interfaces. High porosity metal foams ($\varepsilon > 0.85$) have gained attention in recent years as potentially excellent candidates for meeting the high thermal dissipation demands in the electronic industry. The mechanisms that contribute to the enhanced heat transfer include heat conduction in the metal foam matrix (whose conductivity is usually several orders of magnitude higher compared to the fluid conductivity), and thermal dispersion in the fluid at high velocities. The dispersion conductivity accounts for the effects of pore-level hydrodynamics on the macroscopic transport and essentially represents the enhanced mixing due to the presence of the solid phase.

The well-known Darcy's law is based on a balance between the pressure gradient and the viscous forces and breaks down for high velocities when inertia terms are no longer negligible. Non-Darcy effects become particularly important in metal foams as the fluid moves in tortuous paths and eddies are shed behind the solid fibers in the interstitial pore volume. The resulting pressure drop across the medium and the increased mixing (or dispersion) accounts for an increase in the net transport. Earlier efforts to quantify the effects of dispersion were mostly confined to packed beds. More recent studies for forced convection have shown an increase in heat transfer with the inclusion of thermal dispersion [1–5]. Jiang et al. [6] found that, if thermal dispersion effects are

* Corresponding author. Tel.: +1-517-353-4366; fax: +1-517-353-8787.

E-mail addresses: phani@msu.edu (M.S. Phanikumar), mahajan@spot.colorado.edu (R.L. Mahajan).

0017-9310/02/$ - see front matter
PII: S0017-9310(02)00089-3

Nomenclature

a_{sf}	specific surface area, Eq. (10)
A	area of heat sink base, Eq. (1)
Bi_f, Bi_s	Biot numbers for the fluid and the solid matrix, Eq. (23)
C	geometric factor
C_D	dispersion coefficient, Eq. (15)
Da	Darcy number
d_f, d_p	fiber diameter and pore size
g	gravitational acceleration
h_{sf}	interfacial heat transfer coefficient between solid matrix and fluid
h	heat transfer coefficient
k_d	dispersion conductivity, Eq. (15)
k_{fe}	effective thermal conductivity of fluid
k_{se}	effective thermal conductivity of the solid matrix
k_{eff}	effective thermal conductivity of the porous medium, Eq. (14)
K	permeability of the porous medium
L	length of the porous sample
m	the exponent in Eq. (13)
Nu	Nusselt number, Eq. (25)
p	pressure
Pr	Prandtl number
Q	heat input to the patch heaters
Ra	Rayleigh number
Re_d	Reynolds number based on the fiber diameter
T_{amb}	ambient temperature, Eq. (1)
T_{base}	average temperature of the base, Eq. (1)
T_f, T_s	temperature of fluid and the solid matrix respectively
u, v	horizontal and vertical velocity components
$\mathbf{v}, \tilde{\mathbf{v}}$	velocity vector in the porous medium (dimensional and dimensionless)
x, y	horizontal and vertical Cartesian coordinates

Greek symbols

α	thermal diffusivity
β	coefficient of thermal expansion
δ	Kronecker delta function
ε	porosity of the porous medium
λ_f, λ_s	fluid and solid conductivity ratios
ρ	density
θ_f, θ_s	dimensionless temperatures of fluid and solid
μ	coefficient of dynamic viscosity

Suffixes

eff	effective value for the porous medium
f	fluid
fe	effective value for the fluid
s	solid matrix
se	effective value for the solid matrix
∞	ambient conditions
sf	interfacial conditions
p	denotes pore level conditions

ignored for forced convection in water, then the numerically predicted heat transfer results are lower compared to the experimental results.

The aim of this paper is to present numerical and experimental results for buoyancy-induced flow in a high porosity metal foam heated from below and surrounded by a fluid. Energy transport in porous media is generally studied by invoking the assumption of local thermal equilibrium (LTE). Using this approach, a single equation describes the temperature in the porous medium. Consequently, the temperatures of solid and fluid are assumed equal. The validity of this assumption for metal foams is doubtful due to the vastly different thermal conductivities encountered for the metal foam–fluid combinations. Hence, the effects of local thermal non-equilibrium (LTNE) are studied by using a two-equation model for energy. A two-equation model was used earlier, among others, by Amiri and Vafai [2], Amiri et al. [3], Jiang et al. [6], Nield and Kuznetsov [7], and Calmidi and Mahajan [5]. However, a majority of these investigations reports results for situations in which there are no fluid–porous medium interfaces. To the best of our knowledge, no work has been reported for high-porosity metal foams in which a two-energy equation approach is used in the presence of interfaces. In this paper, we fill this knowledge gap and demonstrate the successful application of such a model in the presence of two interfaces.

2. Experiments

The metal foam heat sinks were tested under natural convection conditions in a horizontal configuration. Photographs of typical metal foam samples are shown in Figs. 1(a) and (b) and a schematic of the experimental setup is shown in Fig. 1(c). A large Plexiglas housing of 0.4572 m in height and width and 0.3048 m deep (perpendicular to the plane of the paper in Fig. 1(c)) stations the sample and keeps it isolated from the ambient. Holes were drilled on the base of the samples to insert Firerod® cartridge heaters. The base of the sample was insulated using low conductivity Styrofoam insulation (5.0 cm in thickness). The area of the insulation block is 16.5 cm × 16.5 cm with the sample placed at the center. The cartridge heaters were powered by a DC power supply. The

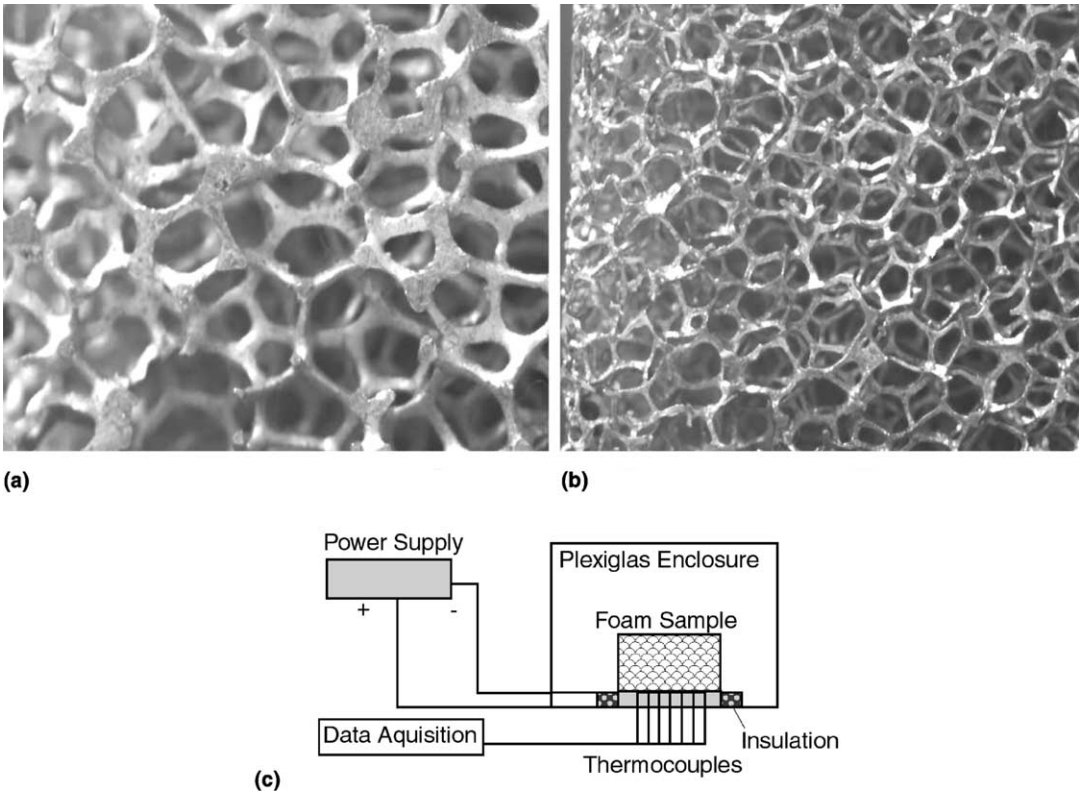

Fig. 1. Metal foam samples used in the experiments showing the relative sizes of pores: (a) 5 PPI; (b) 40 PPI; (c) schematic of the experimental setup.

base and ambient temperatures were monitored using 0.127 mm T-type thermocouples connected to an Omega DASTC data acquisition system. Experiments were conducted on foam samples of different porosities and pore densities. For each pore density corresponding to 5, 10, 20 and 40 PPI, two samples of different porosities were chosen. During a typical experimental run, the power to the heaters was varied to achieve different base plate temperatures and hence Rayleigh numbers. Due to temperature properties of the Styrofoam insulation, our experiments were restricted to maximum base plate temperatures of 75 °C. The heat transfer coefficient for a typical experimental run was calculated based on the following equation:

$$h = \frac{Q}{A(T_{\text{base}} - T_{\text{amb}})}. \tag{1}$$

3. Analysis

Consider a metal foam sample heated from below (Fig. 2). The foam sample is saturated with and surrounded by a fluid, which extends a distance s_1 in the x-direction and s_2 in the y-direction. The steady,

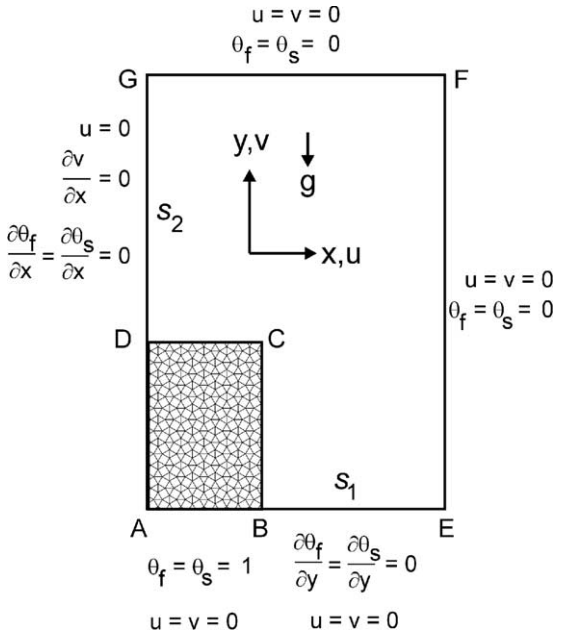

Fig. 2. Definition sketch.

two-dimensional equations for the fluid-saturated porous medium and for the clear fluid region outside the metal foam are written separately as shown below. For the porous medium the governing equations for the non-Darcy model were derived following the well-known volume averaging procedures [8,9]. The energy equations are written using a semi-heuristic approach and are based on a local thermal non-equilibrium (LTNE) model in which the temperature of the solid and the fluid are solved separately.

Continuity and momentum for porous medium:

$$\nabla \cdot \langle \mathbf{v} \rangle = 0, \tag{2}$$

$$\frac{\rho_f}{\varepsilon^2}\langle \mathbf{v} \rangle \cdot \nabla \langle \mathbf{v} \rangle = -\nabla \langle p \rangle^f + \rho_f \mathbf{g} + \frac{\mu}{\varepsilon}\nabla^2 \langle \mathbf{v} \rangle - \frac{\mu}{K}\langle \mathbf{v} \rangle - \frac{C}{K^{1/2}}\rho_f |\langle \mathbf{v} \rangle| \langle \mathbf{v} \rangle. \tag{3}$$

Energy equation for the fluid in the porous medium (*LTNE*):

$$\langle \rho_f \rangle^f c_{pf} \langle \mathbf{v} \rangle \cdot \nabla \langle T_f \rangle^f = \nabla \cdot \{(k_{fe} + k_d) \cdot \nabla \langle T_f \rangle\} + h_{sf} a_{sf} \left(\langle T_s \rangle^s - \langle T_f \rangle^f \right). \tag{4}$$

Energy equation for the solid matrix (*LTNE*):

$$0 = \nabla \cdot \{k_{se} \cdot \nabla \langle T_s \rangle^s\} - h_{sf} a_{sf} \left(\langle T_s \rangle^s - \langle T_f \rangle^f \right). \tag{5}$$

Continuity and momentum for fluid outside porous medium:

$$\frac{\partial u}{\partial x} + \frac{\partial v}{\partial y} = 0, \tag{6}$$

$$\rho_f \left(u\frac{\partial u}{\partial x} + v\frac{\partial u}{\partial y} \right) = -\frac{\partial p}{\partial x} + \frac{\partial}{\partial x}\left(\mu_f \frac{\partial u}{\partial x} \right) + \frac{\partial}{\partial y}\left(\mu_f \frac{\partial u}{\partial y} \right), \tag{7}$$

$$\rho_f \left(u\frac{\partial v}{\partial x} + v\frac{\partial v}{\partial y} \right) = -\frac{\partial p}{\partial y} + \frac{\partial}{\partial x}\left(\mu_f \frac{\partial v}{\partial x} \right) + \frac{\partial}{\partial y}\left(\mu_f \frac{\partial v}{\partial y} \right) + \rho_f g \beta (T - T_\infty). \tag{8}$$

Energy equation for the fluid outside porous medium:

$$\rho_f c_{pf} \left(u\frac{\partial T_f}{\partial x} + v\frac{\partial T_f}{\partial y} \right) = \frac{\partial}{\partial x}\left(k_f \frac{\partial T_f}{\partial x} \right) + \frac{\partial}{\partial y}\left(k_f \frac{\partial T_f}{\partial y} \right). \tag{9}$$

To evaluate the influence of the local thermal equilibrium assumption for metal foams, we have used both the equilibrium and non-equilibrium models for temperature. The energy equations, however, are shown only for the LTNE model. A single energy equation can be easily derived for the limit of thermal equilibrium ($T_f = T_s$), by adding the two Eqs. (4) and (5). In Eq. (3), the last three terms are the Brinkman (or friction) term, the Darcy term and the Forchheimer (or inertia) term. The notation $\langle \phi \rangle$ is used to denote the local volume average of a quantity while $\langle \phi \rangle^\gamma$ denotes the intrinsic phase average of the same quantity for phase γ while the subscripts s and f denote solid and fluid respectively. The effective conductivities for the porous medium, fluid and the solid matrix are k_{eff}, k_{fe} and k_{se} respectively. They are functions of the geometry of the medium and the individual phase conductivities k_s and k_f respectively. C denotes the geometric function, h_{sf} is the interfacial heat transfer coefficient between the solid matrix and the fluid, and a_{sf} is the specific surface area of the foam sample. Since the geometry of metal foams is considerably complex, workable approximations have been derived based on simpler models. For the simplified geometry of an array of parallel cylinders intersecting in the three mutually perpendicular directions, a_{sf} is given by the following expression:

$$a_{sf} = \frac{3\pi d_f}{d_p^2}. \tag{10}$$

The above expression needs to be modified for metal foams to acknowledge the fact that the fibers are non-circular in cross-section. Following Calmidi and Mahajan [5]:

$$a_{sf} = \frac{3\pi d_f}{(0.59 d_p)^2}\left[1 - \exp\left(-\left(\frac{1-\varepsilon}{0.04} \right) \right) \right]. \tag{11}$$

Pore size d_p refers to the size of the pores which are in the shape of a dodecahedron and is usually expressed in units of pores per inch (PPI). The fibers of the metal foam form the edges of a dodecahedron with about 12–14 sides and the cross- section of the fiber is circular only for low porosity values. The porosity ε, the pore size d_p and the fiber diameter d_f are related.

The interfacial heat transfer coefficient for packed beds is usually calculated using a correlation due to Wakao et al. [10]. No such general correlation exists for foamed materials. However, noting that the radial temperature gradients are expected to be small for metal foams, it is reasonable to use an appropriate Nusselt number correlation for flow over an external body to calculate h_{sf}. For the present problem the natural convection velocity $|\langle \mathbf{v} \rangle|$ can be used to calculate a Reynolds number based on the fiber diameter ($= |\langle \mathbf{v} \rangle| \cdot d_f / v \cdot \varepsilon$). The interfacial heat transfer coefficient, h_{sf}, can then be calculated using a forced convection correlation. For all cases considered in the present work, the fiber Reynolds numbers (Re_d) are less than 20,000 although in most cases the Reynolds number is less than 1000. For this range the following correlation proposed by Zhukauskas [11] can be used to estimate h_{sf}:

$$\overline{Nu}_d = \frac{h_{sf} \cdot d_p}{k_f} = \begin{cases} 0.75 Re_d^{0.40}\ Pr^{0.37}, & 1 \leqslant Re_d \leqslant 40, \\ 0.51 Re_d^{0.51}\ Pr^{0.37}, & 40 \leqslant Re_d \leqslant 1000, \\ 0.26 Re_d^{0.60}\ Pr^{0.37}, & 1000 \leqslant Re_d \leqslant 2 \times 10^5. \end{cases} \tag{12}$$

The above correlation is strictly valid for circular cylinders. For metal foams, as pointed out above, the cross-section of the fibers is circular only for low porosity values. As the porosity increases (>0.9), the fiber cross-section changes from being circular to almost triangular. Since interest in the present work is confined to high porosity values, need for a correlation that takes this fact into account is indicated. However, a closer examination of the heat transfer correlations for external flow over bodies of different cross-sections [12] shows that an equation of the form

$$\overline{Nu}_{\mathrm{d}} = C_T \cdot Re_{\mathrm{d}}^{m} Pr^{0.37} \tag{13}$$

can be used for non-circular cross-sections and that the exponent m varies much more slowly compared to the constant C_T. The exponent m was found to lie between 0.5 and 0.78 depending on the cross-section and the Reynolds number. For the fiber Reynolds numbers encountered in the present work, we have decided to study the effect of the fiber cross-section on the heat transfer by replacing Eq. (12) with Eq. (13) and by using different values for C_T while using a constant value of $m = 0.50$ for the exponent. The results of this study are presented in a later section.

The effective conductivities of the solid and the fluid phases (k_{se} and k_{fe}) have been estimated using the relations proposed by Calmidi and Mahajan [13]. For k_{eff}, we have used the following correlation proposed by Bhattacharya et al. [14]

$$k_{\mathrm{eff}} = M[\varepsilon k_{\mathrm{f}} + (1-\varepsilon)k_{\mathrm{s}}] + (1-M)\Big/\left\{\left(\frac{\varepsilon}{k_{\mathrm{f}}} + \frac{1-\varepsilon}{k_{\mathrm{s}}}\right)\right\}. \tag{14}$$

The correlation is based on considerations of series and parallel resistances to heat transfer at the interface and the coefficient M was found to be 0.35 based on experimental data.

In our work, dispersion is treated as an additional contribution to the stagnant diffusive component as shown in Eq. (4) [1,2]. In an earlier analysis, Koch and Brady [15] used ensemble averaging and defined the dispersion as the product of the velocity, fiber thickness and a constant dependent on the porosity. Using this approach, the dispersion coefficient can be written as

$$k_{\mathrm{d}} = \rho c_{\mathrm{p}} C_{\mathrm{D}} \sqrt{K} \cdot |\mathbf{v}|. \tag{15}$$

Since the metal foam matrix is isotropic, we assume that the x and y components of dispersion are equal (i.e., $k_{\mathrm{dx}} = k_{\mathrm{dy}} = k_{\mathrm{d}}$). The coefficient of thermal dispersion C_{D} requires determination and is described later.

The boundary conditions for the above set of equations are shown in Fig. 2. Due to the symmetry in the problem, it is sufficient to solve only one half of the domain. We consider the right half of the domain and consequently, the left edge AG becomes a line of symmetry. No-slip conditions are imposed on the bottom surface (AE) as well as on the sides EF and FG to approximate the conditions in our experiments. The two sets of equations for the fluid and porous regions are coupled at the two interfaces (BC and CD) by the following matching conditions (shown only for the interface BC):

$$T = \varepsilon T_{\mathrm{f}} + (1-\varepsilon)T_{\mathrm{s}}, \tag{16a}$$

$$\begin{aligned} -k_{\mathrm{fe}}\frac{\partial T_{\mathrm{f}}}{\partial x}\bigg|_{x=L^-} &= -k_{\mathrm{f}}\frac{\partial T_{\mathrm{f}}}{\partial x}\bigg|_{x=L^+}, \\ -k_{\mathrm{se}}\frac{\partial T_{\mathrm{s}}}{\partial x}\bigg|_{x=L^-} &= -k_{\mathrm{f}}\frac{\partial T_{\mathrm{f}}}{\partial x}\bigg|_{x=L^+}, \end{aligned} \tag{16b}$$

$$u|_{x=L^-} = u|_{x=L^+}, \tag{16c}$$

$$v|_{x=L^-} = v|_{x=L^+}, \tag{16d}$$

$$p|_{x=L^-} = p|_{x=L^+}, \tag{16e}$$

$$\mu_{\mathrm{eff}}\frac{\partial u}{\partial x}\bigg|_{x=L^-} = \mu\frac{\partial u}{\partial x}\bigg|_{x=L^+}, \tag{16f}$$

$$\mu_{\mathrm{eff}}\left(\frac{\partial v}{\partial x}+\frac{\partial u}{\partial y}\right)\bigg|_{x=L^-} = \mu\left(\frac{\partial v}{\partial x}+\frac{\partial u}{\partial y}\right)\bigg|_{x=L^+}. \tag{16g}$$

A similar set of equations has been used for the interface CD. Conditions (16a) through (16e) express the continuity of temperature, heat flux, normal and tangential velocities and the pressure respectively while conditions (16f) and (16g) match the deviative normal and shear stresses at the interface. Eq. (16g) represents an extension of the shear stress matching condition due to Neale and Nader [16]. In the above equations, μ_{eff} is an effective viscosity of the porous medium and is associated with the Brinkman term in the momentum equation. Determination of μ_{eff} remains an open problem [17]. Results obtained by assuming $\mu_{\mathrm{eff}} = \mu$ were found to be in good agreement with experimental studies [18].

Matching the temperature and heat flux at the interfaces is a non-trivial task when the solid and fluid phase equations are solved separately. Very little work exists in the literature in which heat flux is matched at a fluid–porous interface while using the two-equation model for energy (e.g., [19]). In one scenario, we may assume that the flux from the fluid is in separate balance with the fluid and the solid phase fluxes on the porous side as shown in Eq. (16b). An alternative approach, used in this work, is to use k_{eff}, defined in Eq. (14). Then, the matching conditions at the interface appear as shown below (only the conditions for the x direction are shown; those in the y direction are similar):

$$\begin{aligned} -k_{\mathrm{eff}}\frac{\partial T_{\mathrm{f}}}{\partial x}\bigg|_{x=L^-} &= -k_{\mathrm{f}}\frac{\partial T_{\mathrm{f}}}{\partial x}\bigg|_{x=L^+}, \\ -k_{\mathrm{eff}}\frac{\partial T_{\mathrm{s}}}{\partial x}\bigg|_{x=L^-} &= -k_{\mathrm{f}}\frac{\partial T_{\mathrm{f}}}{\partial x}\bigg|_{x=L^+}. \end{aligned} \tag{17}$$

This approach is found to provide slightly superior results compared to the conditions shown in Eq. (16b). Eq. (17) can be satisfied by specifying the appropriate diffusion coefficients for the energy equations at the interfaces.

4. Dimensionless equations

The governing equations for the fluid and porous regions were solved using a unified one-domain approach. The advantages of such a formulation are that it automatically ensures the satisfaction of the interfacial conditions and does not involve complicated inner iteration loops for values at the interface [18]. Consequently, the two sets of equations for the fluid and the porous regions are combined into one set by using the following binary flag:

$$\delta(x,y)=\begin{cases}1 & \text{for metal foam} \quad (0<\varepsilon<1),\\ 0 & \text{for clear fluid} \quad (\varepsilon=1).\end{cases} \tag{18}$$

We drop the $\langle\phi\rangle$ notation for convenience and make the above equations dimensionless using the following scales: H for length, (T_h-T_∞) for temperature, (α_f/H) for velocity, (H^2/α_f) for time and $H^2/\rho_f\alpha_f^2$ for pressure. The resulting dimensionless equations are shown below.

Combined momentum equations:

$$\frac{1}{\varepsilon^2}\left(u\frac{\partial u}{\partial x}+v\frac{\partial u}{\partial y}\right)=-\frac{\partial p}{\partial x}-\frac{Pr}{Da}u\delta-\frac{C}{\sqrt{Da}}|\tilde{\mathbf{v}}|u\delta+\varepsilon^{-1}Pr\nabla^2u, \tag{19}$$

$$\frac{1}{\varepsilon^2}\left(u\frac{\partial v}{\partial x}+v\frac{\partial v}{\partial y}\right)=-\frac{\partial p}{\partial y}-\frac{Pr}{Da}v\delta-\frac{C}{\sqrt{Da}}|\tilde{\mathbf{v}}|v\delta+\varepsilon^{-1}Pr\nabla^2v+RaPr\theta. \tag{20}$$

Combined energy equations for the fluid and solid matrix:

$$\left(u\frac{\partial\theta_f}{\partial x}+v\frac{\partial\theta_f}{\partial y}\right)=\frac{Bi_f\cdot\lambda_f\cdot\delta}{\sqrt{Da}}(\theta_s-\theta_f)+\frac{\partial}{\partial x}\left[\left\{\delta\left(\lambda_f+C_D\sqrt{Da}\cdot\sqrt{u^2+v^2}\right)+(1-\delta)\right\}\frac{\partial\theta_f}{\partial x}\right]+\frac{\partial}{\partial y}\left[\left\{\delta\left(\lambda_f+C_D\sqrt{Da}\cdot\sqrt{u^2+v^2}\right)+(1-\delta)\right\}\frac{\partial\theta_f}{\partial y}\right], \tag{21}$$

$$(1-\delta)\left(u\frac{\partial\theta_f}{\partial x}+v\frac{\partial\theta_f}{\partial y}\right)=\delta\lambda_s\nabla^2\theta_s+(1-\delta)\nabla^2\theta_f-Bi_s\cdot\lambda_s\delta(\theta_s-\theta_f). \tag{22}$$

The dimensionless quantities appearing in the above equations are defined as shown below:

$$Da=\frac{K}{H^2},\quad Bi_s=\frac{h_{sf}a_{sf}H^2}{k_{se}},\quad Bi_f=\frac{h_{sf}a_{sf}H\sqrt{K}}{k_{fe}},$$
$$Ra=\frac{g\beta H^3(T_h-T_\infty)}{\upsilon_f\alpha_f},\quad Pr=\frac{\upsilon_f}{\alpha_f},\quad \lambda_f=\frac{k_{fe}}{k_f},$$
$$\lambda_s=\frac{k_{se}}{k_f}. \tag{23}$$

In the combined energy equations (21) and (22), θ_f is used to denote the temperature of the fluid both inside and outside the porous medium depending on the spatial location while the diffusion coefficients at the interface are specified to satisfy Eq. (16b). The dimensionless boundary conditions are shown in Fig. 2. The interface matching conditions are not shown in dimensionless form as they can be easily derived from (16a)–(16g). Heat transfer from the heated wall occurs both through the solid phase and the liquid phase. The total heat transfer can be written as

$$q=\overline{h}L\Delta T, \tag{24}$$

$$\overline{Nu}=\frac{\overline{h}L}{k_f}=\int_0^{L/H}\left(\frac{k_{se}}{k_f}\frac{\partial\theta_s}{\partial y}+\frac{k_{fe}}{k_f}\frac{\partial\theta_f}{\partial y}\right)dx=\overline{Nu}_s+\overline{Nu}_f. \tag{25}$$

Although the Nusselt number could be defined based on the effective thermal conductivity of the porous medium, such a definition would not facilitate an easy comparison of enhancement as the effective conductivity changes with changes in the porosity, and the individual phase conductivities. We therefore have chosen to define the Nusselt number based on the thermal conductivity of the fluid to evaluate enhancement with respect to the base case in which there is no metal foam but only a heated plate placed in ambient fluid. When there is no metal foam, the Nusselt number can be defined as

$$\overline{Nu}_0=\frac{\overline{h}_0L}{k_f}=\int_0^{L/H}\frac{\partial\theta_f}{\partial y}\,dx. \tag{26}$$

The enhancement in heat transfer can then be defined as

$$E=\frac{(\overline{Nu}-\overline{Nu}_0)}{\overline{Nu}_0}. \tag{27}$$

5. Numerical method

The system of equations and boundary conditions have been solved using control volume based, semi-implicit methods [20]. The control volume formulation ensures conservation of momentum and energy as well as the continuity of fluxes. The harmonic mean formulation of Patankar [20] was used to describe the diffusion coefficients at the porous–fluid interfaces. This formulation can handle abrupt changes in the properties (such as permeability) across the interface without requiring

an excessively fine grid. A staggered, non-uniform grid was used and the velocity–pressure coupling was handled using the SIMPLER algorithm. The non-uniform grids enabled the placement of fine steps at the porous–fluid interface and at the boundaries. All computations reported in this paper were carried out using a $251(X) \times 291(Y)$ non-uniform grid after carrying out a careful grid dependence study. The variable geometric grid allowed the placement of fine steps (typically of the order of 10^{-5}) near the heated surface. For this level of grid refinement, the uncertainty in the average Nusselt number reported is less than 3%. The size of the computational domain was varied until the Nusselt number did not change by more than 1% with a further increase in the domain size. A dimensionless value of 10.0 ($s_1 = s_2 = 10$) satisfied this criterion and was used for the computations. The stopping criterion for the computations was based on the requirement that the relative error in the variables between two successive iterations must be less than 10^{-6}.

6. Results and discussion

To validate our numerical model, we compared model results with the work of Beckermann et al. [18] for natural convection in a rectangular enclosure in which there is a fluid–porous interface. Although they did not use a two-equation model for temperature, this comparison was carried out to check the correctness of the interface conditions and our implementation using the one-domain approach. We obtained an excellent agreement for the average Nusselt numbers and the temperature profiles [21].

We considered four representative combinations of high porosity foam material and fluid in the present work: nickel in water, aluminum in water, aluminum in air, and Reticulated Vitreous Carbon (RVC) in air. The experiments were carried out using aluminum foams in air. Properties of these metal foams are summarized in Table 1. All computations reported in this paper used the dimensions of the metal foam sample from the experiments −6.35 cm (Length) × 5.08 cm (Height). In dimensionless coordinates, these lengths translate to 1.25 (Length) and 1.0 (Height) respectively. Since we assume symmetry in the x-direction, all computed results show a metal foam sample with dimensions 0.625 (Length) × 1.0 (Height).

Before discussing the numerical simulations, we first present data from the experimental runs in Fig. 3. An important finding is that the heat transfer rate for a given Rayleigh number decreases as the pore density increases from 5 to 40 PPI. This is due to the fact that resistance to flow decreases with an increase in pore size (or a decrease in pore density) resulting in enhanced mixing and heat transfer. Similarly, we notice from Fig. 3

Table 1
Properties of aluminum metal foam samples used in the present work

PPI	Sample no.	Porosity	d_f (m)	d_p (m)	k_{eff} (W/m K)	k_{se} (W/m K)	k_{fe} (W/m K)	K (m^2)	f	Da
5	1	0.899	5.605E−04	4.221E−03	7.733	7.282	0.023	1.989E−07	8.753E−02	7.709E−05
	2	0.93	5.350E−04	4.347E−03	5.357	5.298	0.024	2.069E−07	8.141E−02	8.019E−05
10	1	0.9085	4.428E−04	3.422E−03	7.008	6.670	0.023	1.075E−07	6.872E−02	4.165E−05
	2	0.9386	4.144E−04	3.413E−03	4.711	4.748	0.024	1.171E−07	6.463E−02	4.539E−05
20	1	0.92	3.500E−04	2.784E−03	6.130	5.935	0.024	1.063E−07	1.023E−01	4.117E−05
	2	0.9353	3.321E−04	2.723E−03	4.963	4.959	0.024	1.172E−07	9.823E−02	4.541E−05
40	1	0.9091	2.500E−04	1.935E−03	6.963	6.632	0.023	5.066E−08	8.254E−02	1.963E−05
	2	0.9586	2.094E−04	1.727E−03	3.185	3.443	0.025	5.987E−08	9.126E−02	2.320E−05

that for a given PPI, the heat transfer increases with a decrease in porosity. As porosity decreases, there is more metal content per unit volume and conduction heat transfer in the metal fibers contributes to a net increase in the heat transfer.

The results of model predictions for the 5 PPI metal foam are shown in Figs. 4 and 5. Fig. 4 shows the variation of the local Nusselt number along the heated foam sample. First we notice that there is an order of magnitude difference between the solid and fluid phase Nusselt numbers, which requires the use of a log scale to show a meaningful comparison. The solid phase heat transfer is clearly the dominant mode of heat transport and the fluid phase makes an incremental contribution to the total heat transfer. We also notice that the maximum in the local Nusselt number occurs at the edge of the metal foam sample ($x = 0.625$). The reason for this behavior becomes clear from Fig. 5(a), which shows, for the 5 PPI foam sample, the plots of stream functions and isotherms. There is convergence of flow near the bottom corner of the metal foam (the point B in Fig. 2) where fluid is entrained due to buoyancy. Consequently, the velocity is highest at this point resulting in high local Nusselt numbers. The isotherm plots shown in Fig. 5 show large gradients in temperature at the interface BC. This is a reflection of higher thermal conductivity for aluminum compared to that of air. The gradients at the interface CD are not as predominantly high, primarily because the entrainment is strongest along the interface BC and partly because the fluid is decelerated once it enters the porous foam. The heated fluid eventually leaves from the top. Although not shown in Fig. 4, the temperature gradients in the solid and the fluid are of a comparable magnitude. A much higher value of Nu_s in Fig. 4 is therefore due to the high value of (k_{se}/k_f) in Eq. (25).

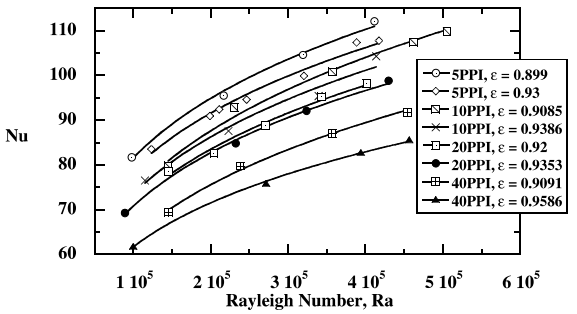

Fig. 3. Summary of experimental heat transfer data.

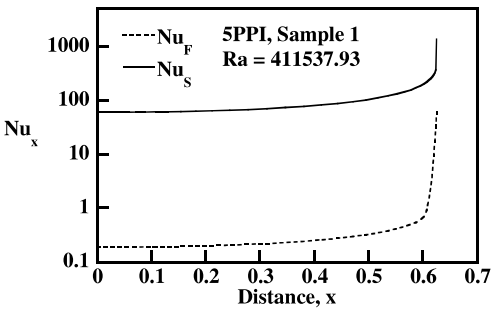

Fig. 4. Local Nusselt number distribution along the heated wall for the 5 PPI metal foam, sample 1.

The computed dimensionless temperature profiles across the interface are shown in Fig. 5(b) for the conditions of the experiment for two different Rayleigh numbers. We notice that, across the interface, the temperature falls steeply from its high value inside the porous medium. The effect of increasing the Rayleigh number is to decrease the temperature in the porous medium due to higher mixing and enhanced heat transfer.

To understand the effect of the empirical constant C_T introduced into the interfacial heat transfer description in Eq. (13) earlier, we carried out numerical simulations for different values of C_T. The results are shown in Fig. 6. As C_T increases, the Nusselt number increases because the efficiency of interfacial heat exchange improves. This trend continues till the solid and fluid phase temperatures satisfy local thermal equilibrium at which point the Nusselt number ceases to increase with a further increase in C_T. This occurs at a value of $C_T = 0.52$. We have used this value for all subsequent computations.

6.1. Comparisons with experimental heat transfer data

Using the value of C_T obtained from the above study we have carried out detailed comparisons between our model predictions and the experimental data for heat transfer. These comparisons are summarized in Fig. 7 for the 5, 10 and 40 PPI samples. The local thermal non-equilibrium (LTNE) model produced an excellent agreement with the experimental data for all the metal foam samples and Rayleigh numbers considered. However, the model based on the LTE assumption significantly underpredicts heat transfer. This difference is about 25% for the 5 PPI sample (Fig. 7). For other samples, we noted larger deviations (not shown in the figure).

Our model for flow is based on the Brinkman–Forchheimer Flow (BFF) model in which we made the assumption that $\mu_e = \mu_f$. Although Givler and Altobelli [17] noted that it is not appropriate to use this assumption for 10 PPI open-cell reticulated foam samples, we found a uniformly good agreement with measured heat transfer data for all the samples – from 5 to 40 PPI. Recently Alazmi and Vafai [22] analyzed the interfacial conditions at a porous–fluid interface and using a single-energy equation for the temperature showed that relations for the effective viscosity such as $\mu_e = 7.5\mu_f$ had

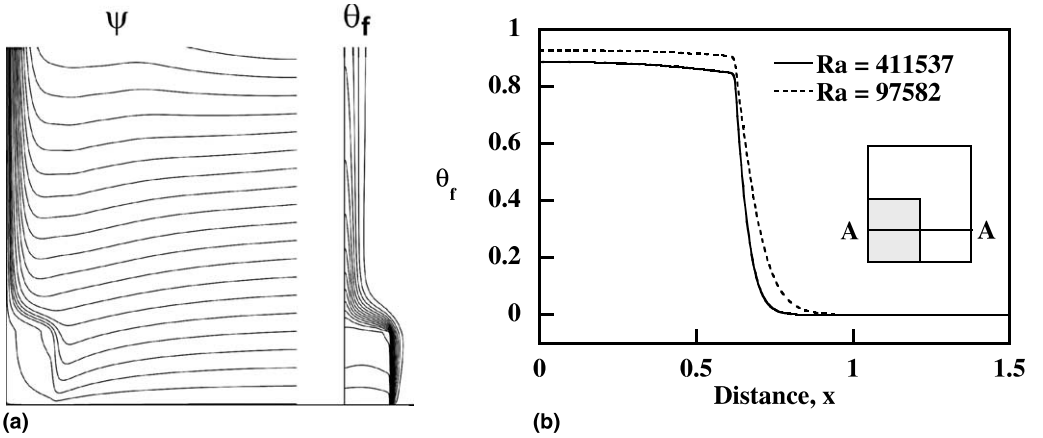

Fig. 5. (a) Streamfunction and isotherm plots for 5PPI metal foam, sample 1, $Ra = 97582$; (b) fluid temperature profiles for different Ra along the transect A–A at $y = 0.5$.

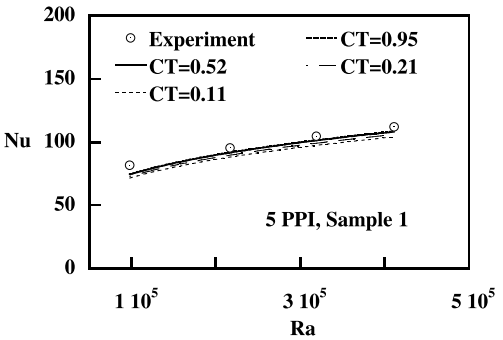

Fig. 6. Effect of the parameter CT on heat transfer results for 5 PPI metal foam.

little effect on the predicted temperature and Nusselt numbers. Our experience, based on the limited sets of metal foam samples and fluids considered in this work, indicates that descriptions of the interfacial heat transfer phenomena while using a two-equation energy model are more important than issues related to the uncertainty in the effective viscosity of the BFF model. The maximum difference between the predictions of the LTNE model and the experimental data is less than 15% for all the cases reported in this paper. Factors that contributed to this difference could potentially include differences in the flow structure between the model (two-dimensional) and the experiment (three-dimensional) in the vicinity of the metal foam and uncertainty in the effective viscosity of the BFF model. The deviation

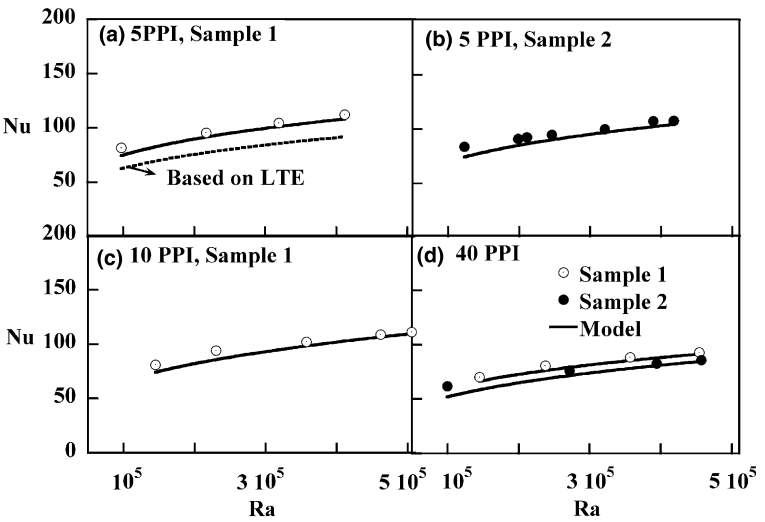

Fig. 7. Comparison of model predictions with experimental data.

between the model and data is highest for the lowest Rayleigh numbers, which is likely related to a higher uncertainty in the measurements for low Rayleigh numbers.

While comparing the model predictions with experimental data we have evaluated the effects of thermal dispersion for the various metal foam–fluid combinations. We found the effects of dispersion to be negligibly small. In particular, for the aluminum metal foams in air, we were not able to assign a meaningful value for the dispersion coefficient C_D as the changes in the mean Nusselt number due to dispersion are significantly lower compared to the uncertainty in our numerical model. Consequently, we have decided to use a value of $C_D = 0.06$ used by Calmidi and Mahajan [5] for similar foam–fluid combinations. For thermal dispersion to become significant, the contribution due to dispersion should be comparable to the effective stagnant conductivity, k_{eff}. Eq. (15) can be rewritten in a dimensionless form as

$$\frac{k_d}{k_{eff}} = \frac{C_D\sqrt{Da}}{\lambda_{eff}}\left|\tilde{\mathbf{v}}\right|. \tag{28}$$

For the aluminum metal foam sample in air, typical values of Da and $|\tilde{\mathbf{v}}|$ (for a Rayleigh number of 411538) are 7.7×10^{-5} and 30 respectively. For C_D values of 0.1 and 0.3, and $\lambda_{eff} = 281.5$, the dispersion accounts for 0.009% and 0.027% of the total stagnant conductivity respectively. Consequently, we expect the effects of thermal dispersion to be negligible for this case. This was indeed borne out by our numerical solutions. However, if we increase the Darcy number (for example, by increasing the height H of the porous block), then the effects of dispersion become important. For example, for a Darcy number of 0.01, thermal dispersion could account for a 10% increase in heat transfer for $C_D = 0.3$. Still higher increases in heat transfer have been obtained for higher Ra. Similarly, we found that effects of thermal dispersion become more pronounced when the saturating fluid is water rather than air.

6.2. Effect of Darcy number

We studied the effect of Darcy number to illustrate the influence of changing the permeability of the porous medium. Fig. 8 shows the streamfunction and isotherm plots for two different values of Darcy number ($Da = 10^{-8}$ and 7.7×10^{-5}). The general conclusion based on these plots is that increasing Da (permeability) helps the flow to penetrate deeper into the porous layer. For example, the low Darcy number results in Fig. 8(a) show that, although the Rayleigh number is relatively high, the flow is unable to penetrate deeper into the porous block due to the high resistance. Consequently, fluid is mostly confined to the region outside the porous sample.

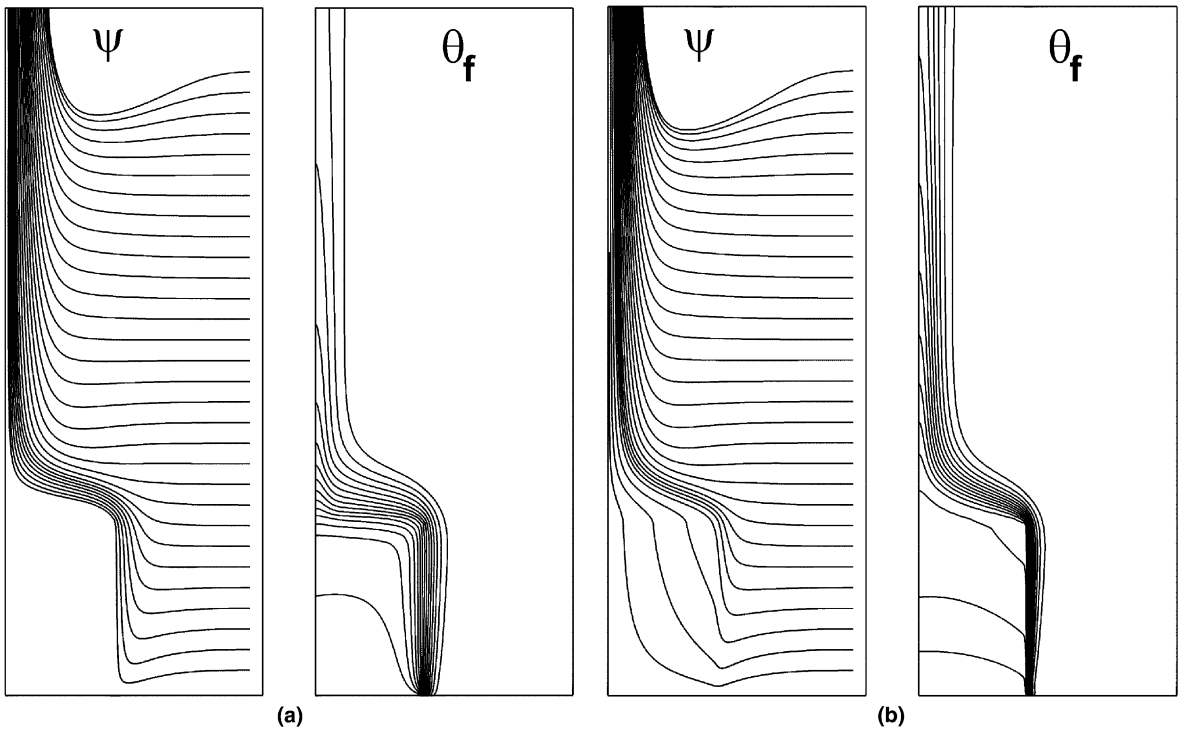

Fig. 8. Effect of Darcy number on flow and temperature fields for $Ra = 411537$ (5 PPI, Sample 1): (a) $Da = 10^{-8}$; (b) $Da = 10^{-3}$.

As Darcy number increases, the flow penetrates deeper into the porous medium as seen from the velocity and temperature fields (Fig. 8(b)). The isotherms show the presence of relatively stronger gradients at the interface. These descriptions are consistent with the fact that for high values of *Da*, the Darcy term becomes small while the Brinkman term in the momentum equation becomes small for low values of *Da*. The influence of Darcy number on the Nusselt number is shown in Fig. 9. The temperature inside the porous foam is much higher for the lower Darcy number due to the lack of mixing as fluid is not able to penetrate inside the block. The Nusselt number increases with Darcy number as noted above while it approaches a constant value for very low values of *Da*. The low *Da* heat transfer asymptote represents the physical limit of an almost impervious porous block.

6.3. Enhancement in heat transfer

To understand the heat transfer enhancement characteristics of different metal foams and fluids, we carried out a parametric study in which we fixed the geometry related properties (such as fiber diameter and pore size) of the metal foam and changed only the properties of the individual phases. We consider the 5 PPI metal foam sample no. 1 shown in Table 1 to illustrate the effect of using various metal foam–fluid combinations. The properties of the fluids and metals are summarized in Table 2. We notice from Table 2 and from Eq. (14) that the effective conductivities of the carbon metal foam are much smaller compared to those for aluminum foam. As a result, the conduction heat transfer which is the dominant mode of transport, will not be as effective for carbon metal foams. The isotherm plot for the carbon–air combination (figure not shown) is marked by the absence of steep temperature gradients at the interface unlike the isotherms shown in Fig. 5 for aluminum–air.

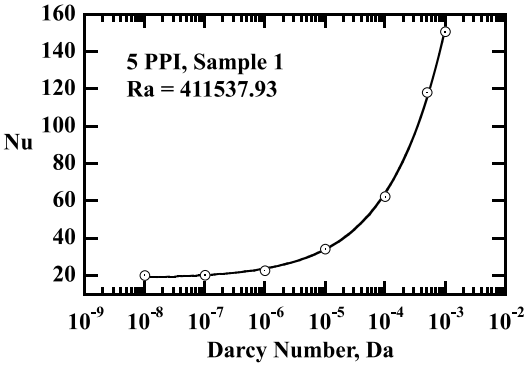

Fig. 9. Effect of Darcy number on heat transfer: 5 PPI, sample 1.

Table 2
Properties of fluids/metals used

Fluid/metal foam	Thermal conductivity (W/m^2 K)	Kinematic viscosity (m^2/s)
Water	0.615	8.00E − 07
Air	0.026	1.59E − 05
Aluminum	218	–
Nickel	90	–
RVC (carbon)	8.5	–

To quantify the heat transfer enhancement, we compared the Nusselt numbers to a base case in which there is no metal foam but only a heated plate placed in ambient fluid. *Nu* for this case is calculated using the following correlation proposed by Lloyd and Moran [23] for a heated surface facing upward:

$$\overline{Nu}_0 = \frac{\overline{h}_0 L}{k_f} = 0.54 Ra_{L^*}^{0.25}, \tag{29}$$

where L^* is a characteristic length of the plane surface. Our results show that although the Nusselt number values are lower for water (due to its high thermal conductivity which appears in the denominator in the definition of *Nu* in Eq. (25)), the enhancement values are higher due to its higher heat capacity. In a limited range of Rayleigh numbers used to carry out this parametric study ($10^5 \leqslant Ra \leqslant 5 \times 10^5$), heat transfer enhancement is almost independent of the Rayleigh number. The aluminum foams in water produce the highest enhancement ($E \approx 16$) followed by nickel–water ($E \approx 9.5$), and then by aluminum–air ($E \approx 3.8$). Carbon metal foams in air do not produce an enhancement.

Heat transfer enhancement in metal foams is the result of a balance between convection in the fluid and conduction in the metal foam matrix. For a given Rayleigh number, the conduction heat transfer due to the presence of a metal foam will have to exceed that due to convection alone (in the absence of metal foam) to obtain an enhancement. This is possible only when the metal foam has a relatively high thermal conductivity compared to that of the fluid. We can postulate the existence of a critical conductivity ratio (as a function of the Rayleigh number) below which no enhancement can be obtained. An example of such a situation is illustrated by RVC-air samples for which the enhancements were found to be less than zero indicating that the metal foam actually contributed to a reduction in heat transfer. This wide range of values for the enhancement can be understood by examining the solid to fluid thermal conductivity ratios (λ_s) for these cases. Carbon has the lowest conductivity among all the metals considered in this study. Our results indicate that when solid conductivity falls below a certain value, use of metal

foams could potentially contribute to a reduction in heat transfer. This can be attributed to the inhibition of flow due to natural convection in the presence of the metal foam matrix (which increases flow resistance). High solid to fluid conductivity ratios are required to overcome this resistance and produce heat transfer enhancement.

6.4. Effects of local thermal non-equilibrium

We examined the effects of local thermal non-equilibrium by comparing the fluid and solid temperatures at every point in the porous medium. The departure of the solid temperature from its fluid counterpart is taken as a measure of the local thermal non-equilibrium as defined below [2]:

$$\%\mathrm{LTNE} = |\theta_s - \theta_f| \times 100. \tag{30}$$

Fig. 10 shows the variation of %LTNE as a function of space for aluminum–air, sample 1. The flow and temperature fields are shown in Fig. 5(a). We notice that the location where the %LTNE is highest is at the point where the velocities are highest. A velocity profile showing the variation of the horizontal velocity (u) along the y- direction (not shown) confirmed that a maximum in the absolute value of velocity indeed occurs near the bottom of the block (point B in Fig. 2). As a result and as expected, we conclude that the LTE assumption becomes invalid in regions where velocities are high.

We found that the LTE assumption is better justified when water is used in place of air. This is due to the much higher conductivity and heat capacity of water which results in a more uniform temperature distribution between the phases. For the same conditions shown in Fig. 10, the aluminum–water combination produced a maximum LTNE of 7.4% compared to a value of 16% for aluminum–air. Examination of a large number of cases showed that the %LTNE increases with the Rayleigh number as well as the Darcy number. When Darcy number increases, flow experiences less resistance to cross over to the porous side. This results in higher fiber Reynolds numbers and larger differences in solid and fluid temperatures. Clearly, an approach based on a single energy equation introduces significant errors in such a situation. In some cases LTNE departures as high as 60% were obtained resulting in potentially significant errors if a single energy equation is employed. Based on this study, we conclude that, for metal foams in general, the two-equation temperature model should be used in place of the traditional one-equation models. Some of the above conclusions may not apply to situations in which there are no fluid–porous interfaces.

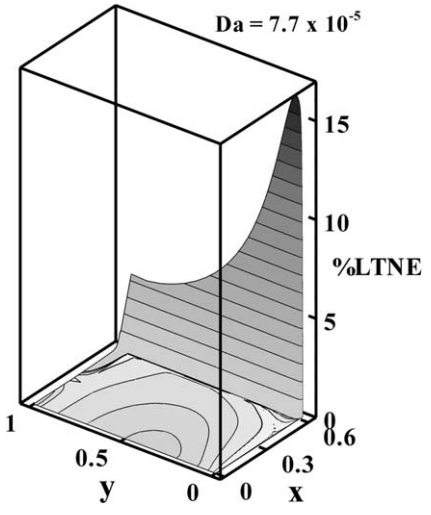

Fig. 10. Local thermal non-equilibrium effects for the 5 PPI aluminum metal foam in air for $Ra = 411537.73$.

7. Conclusions

In this paper, we have examined the flow and heat transfer characteristics of metal foam samples heated from below. By using a two-equation model for the temperature and by integrating the porous medium and the clear fluid domains using the single-domain approach, we were able to successfully predict heat transfer in aluminum metal foams for a wide range of Rayleigh numbers and pore sizes. The predictions based on the non-equilibrium model for temperature are in better agreement with our experimental data compared to those based on the LTE model. Significant enhancements in heat transfer result from the use of metal foams (up to a factor of 4 for Al–air and about 16 for Al–water). Although dispersion did not play a role for the conditions described in this paper, we showed that significant errors could potentially result if dispersion is neglected at high Darcy numbers. Local thermal non-equilibrium effects were found to be significant at high Rayleigh and Darcy numbers and significant errors are introduced if a single-equation approach is adopted. Consequently, we conclude that the two-equation energy model is a better model when fluid porous interfaces are involved and for the metal foam fluid combinations considered in the present work.

Acknowledgements

The authors gratefully acknowledge the help received from Mr. A. Bhattacharya, Department of Mechanical Engineering and CAMPMode, University of Colorado in providing the experimental data.

References

[1] M.L. Hunt, C.L. Tien, Effects of thermal dispersion on forced-convection in fibrous media, Int. J. Heat Mass Transfer 31 (3) (1988) 301–309.

[2] A. Amiri, K. Vafai, Analysis of dispersion effects and non-thermal equilibrium, non-darcian, variable porosity incompressible flow through porous media, Int. J. Heat Mass Transfer 37 (6) (1999) 939–954.

[3] A. Amiri, K. Vafai, T.M. Kuzay, Effects of boundary conditions on non-Darcian heat transfer through porous media and experimental comparisons, Numer. Heat Transfer A 27 (1995) 651–664.

[4] S.W. Hsiao, Natural convection in an inclined porous cavity with variable porosity and thermal dispersion effects, Int. J. Numer. Methods Heat Fluid Flow 8 (1) (1998) 97.

[5] V.V. Calmidi, R.L. Mahajan, Forced convection in high porosity metal foams, ASME J. Heat Transfer 122 (2000) 557–565.

[6] P.-X. Jiang, Z.-P. Ren, B.-X. Wang, Numerical simulation of forced convection heat transfer in porous plate channels using thermal equilibrium and nonthermal equilibrium models, Numer. Heat Transfer A 35 (1999) 99–113.

[7] D.A. Nield, A.V. Kuznetsov, Local thermal nonequilibrium effects in forced convection in a porous medium channel, Int. J. Heat Mass Transfer 42 (1999) 3245–3252.

[8] S. Whitaker, Advances in the theory of fluid motion in porous media, Ind. Eng. Chem. 61 (1968) 14–28.

[9] K. Vafai, C.L. Tien, Boundary and inertia effects on flow and heat transfer in porous media, Int. J. Heat Mass Transfer 24 (1981) 195–203.

[10] N. Wakao, S. Kaguei, T. Funazkri, Effect of fluid dispersion coefficients on particle to fluid heat transfer coefficients in packed beds, Chem. Eng. Sci. 34 (1979) 325–336.

[11] A. Zhukauskas, in: Heat Transfer from Tubes in Cross Flow, Advances in Heat Transfer, vol. 8, Academic Press, New York, 1972.

[12] F.P. Incropera, Introduction to Heat Transfer, Wiley, New York, 1997.

[13] V.V. Calmidi, R.L. Mahajan, The effective thermal conductivity of high porosity fibrous metal foams, ASME J. Heat Transfer 121 (1999) 466–471.

[14] A. Bhattacharya, V.V. Calmidi, R.L. Mahajan, Thermophysical properties of high porosity metal foams, Int. J. Heat Mass Transfer 45 (2002) 1017–1031.

[15] D.L. Koch, J.F. Brady, The effective diffusivity of porous media, AIChE J. 32 (1986) 575.

[16] G. Neale, W. Nader, Practical significance of Brinkman's extension of Darcy's law, Can. J. Chem. Eng. 52 (1974) 475–478.

[17] R.C. Givler, S.A. Altobelli, A determination of the effective viscosity for the Brinkman–Forchheimer flow model, J. Fluid Mech. 258 (1994) 355–370.

[18] C. Beckermann, S. Ramadhyani, R. Viskanta, Natural convection flow and heat transfer between a fluid layer and porous layer inside a rectangular enclosure, ASME J. Heat Transfer 109 (1987) 363–370.

[19] M.L. Martins-Costa, R.M. Saldanha da Gama, A local model for the heat transfer process in two distinct regions, Int. J. Heat Fluid Flow 15 (6) (1994) 477–485.

[20] S.V. Patankar, Numerical Heat Transfer and Fluid Flow, Hemisphere, Washington, DC, 1980.

[21] M.S. Phanikumar, R.L. Mahajan, Non-Darcy natural convection in a high-porosity metal foam heated from below: effects of thermal dispersion and local thermal non-equilibrium, Parts 1 and 2, in: Proceedings of the 8th Brazilian Thermal Engineering Conference, Porto Alegro, Brazil, 2000, p. 136, 138.

[22] B. Alzami, K. Vafai, Analysis of flow and heat transfer interfacial conditions between a porous medium and a fluid layer, Int. J. Heat Mass Transfer 44 (2001) 1735–1749.

[23] J.R. Lloyd and W.R. Moran, Natural convection adjacent to horizontal surfaces of various planforms, ASME Paper 74-WA/HT-66, 1974.